Materials & Design 268 (2026) 116404

Contents lists available at ScienceDirect

Materials & Design

journal homepage: www.elsevier.com/locate/matdes

An origin of superelasticity in Fe–Mn–Al–Ni alloy: A phase-field study

Miyu Takagi [a], Yuhki Tsukada [a,*], Toshiyuki Koyama [b], Dasom Kim [a], Naoki Takata [a]

[a] Department of Materials Design Innovation Engineering, Graduate School of Engineering, Nagoya University, Furo-cho, Chikusa-ku, Nagoya 464-8603, Japan
[b] Research Center for Structural Materials, National Institute for Materials Science, 1-2-1, Sengen, Tsukuba, Ibaraki 305-0047, Japan

ARTICLE INFO

Keywords:
Phase-field model
Martensitic transformation
Superelasticity
Nanoprecipitate
Free-energy change

ABSTRACT

Phase-field simulations are performed to investigate the martensitic transformation (MT) from body-centered-cubic-α to face-centered-cubic-γ′ when external compressive stress is applied along the $[100]_\alpha$ direction, as well as the reverse MT from γ′ to α during the unloading of the external stress. The objective is to gain fundamental insights into the reversibility of the MT in Fe–Mn–Al–Ni alloy with a microstructure containing nanoscale β-NiAl precipitates in the α phase. The stress-induced MT from α to γ′ occurred under a compressive loading of approximately 400 MPa, resulting in a martensite microstructure composed of two of the three crystallographic orientation variants. The elastic energy in the β phase increased owing to the MT, which slightly increased the structural density of martensite and consequently increased the chemical free energy of the β phase. Moreover, the structural density of martensite in the γ′ phase decreased near the β-phase boundary, where a compositional gradient was present, resulting in an increase in the chemical free energy of the γ′ phase. A complete reverse MT occurred when the total free-energy change, determined by the balance between the elastic-energy change and chemical free-energy change, temporarily became positive during the unloading of external stress.

1. Introduction

Shape-memory alloys (SMAs), represented by Ni–Ti alloys, exhibit excellent properties such as the shape-memory effect and superelasticity, and have been used in various applications including medical devices and actuators [1]. The development of SMAs based on other alloy systems has also been pursued to overcome the limitations of Ni–Ti alloys, such as low ductility, poor cold formability, and high material costs [2]. Ferrous SMAs such as Fe–Mn–Si [3,4] and Fe–Ni–Co–Ti (FNCT) alloys [5] have gained attention owing to their low material costs, high ductility, and ease of thermomechanical processing. However, the superelastic (SE) strain obtained is not sufficient for their practical use because most ferrous SMAs undergo a non-thermoelastic martensitic transformation (MT) instead of a thermoelastic MT.

Tanaka et al. [6] developed a ferrous SMA, boron-doped Fe–Ni–Co–Al–Ta (FNCAT) alloy, exhibiting a large SE strain of over 13% at room temperature. In the FNCAT alloy microstructure, the ordered $(Ni,Fe,Co)_3(Al,Ta)$ phase with $L1_2$ structure coherently precipitates in the γ parent phase with a disordered face-centered cubic (fcc-A1) structure, enabling the thermoelastic MT from the γ phase to α′ phase (with body-centered cubic (bcc) or body-centered tetragonal (bct) structure) under tensile-stress loading [6], or contributing to achieving an excellent balance of strength and ductility [7]. The formation of the $L1_2$-ordered phase in the γ phase has also been confirmed in boron-doped Fe–Ni–Co–Al–Ti alloy that exhibits superelasticity [8–11]. Omori et al. [12] developed ferrous SMAs by adding Ni to Fe–Mn–Al alloy, which undergoes a non-thermoelastic MT [13]. The addition of Ni induces the coherent precipitation of the ordered β-NiAl phase with B2 structure in the α parent phase with a disordered bcc-A2 structure, triggering the thermoelastic MT of α to γ′ (with fcc structure) and resulting in the excellent SE response of Fe–Mn–Al–Ni (FMAN) alloys. The remarkable features of the developed Fe–34Mn–15Al–7.5Ni (at.%) alloy are as follows: (1) it exhibits superelasticity over a wide temperature range from –196 to 240 °C [12], (2) the temperature dependence of the critical stress for inducing the MT is one order of magnitude smaller than that of conventional SE alloys [12,14,15], and (3) it has a large stress hysteresis [12,16]. Therefore, this alloy is considered promising as a vibration-damping material for civil-engineering structures [17].

Tseng et al. [14,18] conducted tensile and compression tests along the [001] direction of Fe–34Mn–15Al–7.5Ni single-crystal alloy to investigate its SE response. The compression-deformed samples exhibited large recoverable strains; however, the tension-deformed samples showed large irrecoverable strains and contained significant amounts of

* Corresponding author.
E-mail address: tsukada.yuhki@material.nagoya-u.ac.jp (Y. Tsukada).

https://doi.org/10.1016/j.matdes.2026.116404
Received 11 March 2026; Received in revised form 13 May 2026; Accepted 12 June 2026
Available online 14 June 2026

retained martensite. Two of the three crystallographic orientation variants (OVs) of martensite are formed under compressive-stress loading owing to the anisotropy in the transformation strain, and the resulting multivariant structure is considered effective in relaxing the internal elastic energy associated with the MT under the external stress loading. In contrast, under tensile-stress loading, only a single OV of martensite is formed, which is considered the reason for the higher dislocation densities and smaller recoverable strains of the tensile-deformed samples compared with the compression-deformed samples [14]. The effects of crystallographic orientation on the SE properties of FMAN alloy have also been investigated [18–20]. Bauer et al. [19] conducted tensile tests of Fe–34Mn–15Al–7.5Ni oligocrystalline alloy to investigate the effect of grain orientations and grain boundaries on the SE response of the alloy. The decrease in the reversibility of MT was owing to the detwinning of twinned martensite under tensile-stress loading and the formation of irreversible martensite induced by stress concentrations at grain boundaries.

In ferrous FNCT, FNCAT, and FMAN alloys, the nanoscale ordered phase coherently precipitated in the parent phase is assumed to strengthen the austenite phase and hinder slip deformation, thereby enabling a thermoelastic MT. In FNCT alloys, nanoscale Ni_3Ti with $L1_2$ structure coherently precipitates in the γ parent phase with an fcc-A1 structure during aging. The shape-memory properties of FNCT alloys, such as recoverability and temperature hysteresis, vary depending on the aging heat-treatment conditions [21–23]. Similarly, Ma et al. [24] varied the aging time of FNCAT alloys to change the size of nanoscale $(Ni,Fe,Co)_3(Al,Ta)$ precipitates in the γ phase, demonstrating that the precipitate size significantly affects the SE properties including SE strain, stress hysteresis, and the slope of the SE stress–temperature diagram. Furthermore, Tseng et al. [16] demonstrated that the SE properties of FMAN alloys, such as SE strain and stress hysteresis, can be optimized by controlling the size of the nanoscale β phase in the α phase through aging heat treatments. La Roca et al. [25] investigated the effect of the nanoprecipitation of the β phase on the relative stability between the austenite (α) and martensite (γ′) in FMAN alloys. They conclude that increases in the size and volume fraction of the precipitates suppress the thermally-induced MT. Observation of the β phase in FMAN alloys using high-angle annular dark-field scanning transmission electron microscopy showed that the β precipitates are distorted in the γ′ phase, but still have coherent interfaces with the γ′ phase [26]. The internal elastic energy associated with the coherent precipitation of the β phase may act as the driving force for the reverse MT from γ′ to α [25,26].

Several insights regarding the relationship between the microstructure and properties of ferrous SMAs have been obtained through experimental studies; however, the specific role of nanoscale precipitates remains unclear. In the present study, the MT from α to γ′ under external stress loading and reverse MT from γ′ to α during external stress unloading are simulated based on the phase-field method to clarify the role of nanoscale β precipitates in the reversibility of the MT in Fe–34Mn–15Al–7.5Ni single-crystal alloy having an α + β two-phase microstructure. The Gibbs energy of the constituent phases calculated using the calculation of phase diagrams (CALPHAD) database [27] is incorporated into the phase-field model. Furthermore, in the phase-field model, the elastic energy is formulated considering the coherent precipitation of the β phase in the α phase and bcc-to-fcc transformation strain associated with the MT from α to γ′. This study aims to gain fundamental insights into the reversibility of the MT from the perspective of free-energy changes. Therefore, for simplicity, the elastic energy is formulated without considering the loss of coherency of the β precipitates and plastic deformation during the MT and reverse MT.

2. Calculation method

2.1. Phase-field model

Two types of field variable are defined to simulate the MT from α to γ′ in the Fe–34Mn–15Al–7.5Ni single-crystal alloy having an α + β two-phase microstructure. The first field variable is the normalized composition $c(\boldsymbol{r},t)$ in a pseudo-binary system, which takes a value of 1 at the β-phase composition, 0 at the α-phase composition, and $0 < c < 1$ at the boundary between the β and α phases (see Section 2.2 for detail). The second field variable is the long-range order parameters $\phi_i(\boldsymbol{r},t)$, where $i = 1, 2, 3$, which represents the three crystallographic OVs of martensite (γ′). $\phi_i(\boldsymbol{r},t)$ represents the structural density of the three OVs; $\phi_i(\boldsymbol{r},t)$ takes a value of 1 inside the domain of the i-th OV, 0 outside the domain of the i-th OV, and $0 < \phi_i < 1$ at the OV domain boundary. Fig. 1 shows the lattice correspondence between bcc-α and fcc-γ′ in bcc-to-fcc MT. OV1, OV2, and OV3 are defined such that $[0\,0\,1]_{\gamma'}$ coincides with $[1\,0\,0]_{\alpha}$, $[0\,1\,0]_{\alpha}$, and $[0\,0\,1]_{\alpha}$, respectively.

The temporal evolution of the field variables is as follows:

$$\frac{\partial c(\boldsymbol{r},t)}{\partial t} = \nabla\left(M\nabla\frac{\delta G_{\mathrm{sys}}}{\delta c(\boldsymbol{r},t)}\right) \tag{1}$$

$$\frac{\partial \phi_i(\boldsymbol{r},t)}{\partial t} = -L\frac{\delta G_{\mathrm{sys}}}{\delta \phi_i(\boldsymbol{r},t)} \tag{2}$$

where G_{sys} is the total free energy of the system, M is the diffusion mobility, and L is the structural relaxation coefficient [28]. G_{sys} is a functional of the field variables and is defined by

$$G_{\mathrm{sys}} = G_{\mathrm{chem}} + E_{\mathrm{grad}} + E_{\mathrm{str}} \tag{3}$$

where G_{chem} is the chemical free energy, E_{grad} is the gradient energy, and E_{str} is the elastic strain energy. G_{chem} can be written as a Landau-type polynomial as follows [29]:

$$G_{\mathrm{chem}} = \int_{\boldsymbol{r}} g_{\mathrm{chem}}\mathrm{d}\boldsymbol{r} \tag{4}$$

$$\begin{aligned} g_{\mathrm{chem}} = {} & \frac{A_2}{2}(c-1.0)^2 + \frac{A_4}{4}c^2(c-1.0)^2 + \frac{A_8}{2}c^2(c-1.0)^6 \\ & + \frac{B_2}{2}(c_+ - c)\sum_{i=1}^{3}\phi_i^2 - \frac{B_3}{3}\sum_{i=1}^{3}\phi_i^3 + \frac{B_4}{4}\left(\sum_{i=1}^{3}\phi_i^2\right)^2 \end{aligned} \tag{5}$$

where A_2, A_4, A_8, c_+, B_2, B_3, and B_4 are constants determined based on the Gibbs energy of the constituent phases. E_{grad} is given by

$$E_{\mathrm{grad}} = \int_{\boldsymbol{r}}\left\{\kappa_c(\nabla c)^2 + \frac{\kappa_\phi}{2}\sum_{i=1}^{3}(\nabla\phi_i)^2\right\}\mathrm{d}\boldsymbol{r} \tag{6}$$

where κ_c and κ_ϕ are the gradient-energy coefficients. E_{str} is calculated based on phase-field microelasticity theory [30]:

$$E_{\mathrm{str}} = E_{\mathrm{el}} + E_{\mathrm{pot}} \tag{7}$$

$$E_{\mathrm{el}} = \int_{\boldsymbol{r}} e_{\mathrm{el}}\mathrm{d}\boldsymbol{r} \tag{8}$$

$$e_{\mathrm{el}} = \frac{1}{2}C_{ijkl}(\boldsymbol{r},t)\left\{\varepsilon_{ij}(\boldsymbol{r},t) - \varepsilon^0_{ij}(\boldsymbol{r},t)\right\}\left\{\varepsilon_{kl}(\boldsymbol{r},t) - \varepsilon^0_{kl}(\boldsymbol{r},t)\right\} \tag{9}$$

$$E_{\mathrm{pot}} = -V\sigma^{\mathrm{appl}}_{ij}\bar{\varepsilon}_{ij} \tag{10}$$

where E_{el} is the internal elastic energy, E_{pot} is the potential energy of the applied external stress (the work done by the loading device), C_{ijkl} is the elastic modulus, ε_{ij} is the total strain, ε^0_{ij} is the eigenstrain, V is the system volume, $\sigma^{\mathrm{appl}}_{ij}$ is the applied external stress, and $\bar{\varepsilon}_{ij}$ is the uniform macroscopic strain defined as $\bar{\varepsilon}_{ij} \equiv \int_{\boldsymbol{r}}\varepsilon_{ij}\mathrm{d}\boldsymbol{r}/V$. For simplicity, an elastically homogeneous system is assumed, i.e., C_{ijkl} is constant. The body is allowed to relax at a fixed $\sigma^{\mathrm{appl}}_{ij}$ (stress-controlled boundary condition), and $\bar{\varepsilon}_{ij}$ is determined such that E_{str} is minimized with respect to $\bar{\varepsilon}_{ij}$. ε_{ij} is

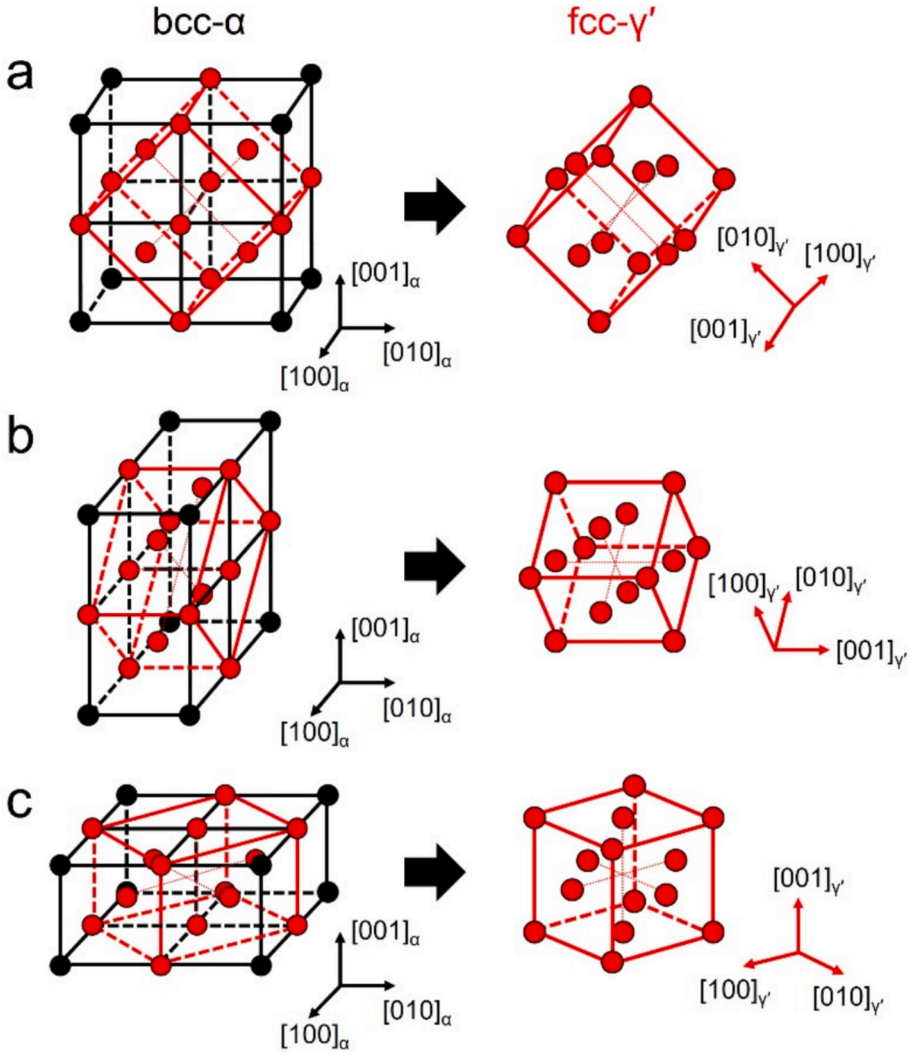

Fig. 1. Lattice correspondences between bcc-α (black) and fcc-γ′ (red) in bcc-to-fcc MT: (a) OV1, (b) OV2, and (c) OV3. (For interpretation of the references to colour in this figure legend, the reader is referred to the web version of this article.)

obtained by solving the mechanical-equilibrium equation ($\partial\sigma_{ij}/\partial r_j = 0$, $\sigma_{ij} = C_{ijkl}\{\varepsilon_{kl}(\boldsymbol{r},t) - \varepsilon^0_{kl}(\boldsymbol{r},t)\}$) in Fourier space. The eigenstrain is defined as follows:

$$\varepsilon^0_{kl} = \varepsilon_0\delta_{kl}c(\boldsymbol{r},t) + \sum_{i=1}^{3}\varepsilon^{(i)}_{kl}\phi_i(\boldsymbol{r},t) \tag{11}$$

where ε_0 is the lattice misfit calculated from the lattice parameters of the α and β phases as $\varepsilon_0 = (a_\beta - a_\alpha)/a_\alpha$, δ_{ij} is the Kronecker delta function, and $\varepsilon^{(i)}_{kl}$ is the transformation strain of the bcc-to-fcc MT for the i-th OV. $\varepsilon^{(i)}_{kl}$ is given by

$$\left[\varepsilon^{(1)}_{kl}\right] = \begin{pmatrix} \varepsilon_c & 0 & 0 \\ 0 & \varepsilon_a & 0 \\ 0 & 0 & \varepsilon_a \end{pmatrix}, \left[\varepsilon^{(2)}_{kl}\right] = \begin{pmatrix} \varepsilon_a & 0 & 0 \\ 0 & \varepsilon_c & 0 \\ 0 & 0 & \varepsilon_a \end{pmatrix}, \left[\varepsilon^{(3)}_{kl}\right] = \begin{pmatrix} \varepsilon_a & 0 & 0 \\ 0 & \varepsilon_a & 0 \\ 0 & 0 & \varepsilon_c \end{pmatrix} \tag{12}$$

where $\varepsilon_a = (a_{\gamma'} - \sqrt{2}a_\alpha)/\sqrt{2}a_\alpha$ and $\varepsilon_c = (a_{\gamma'} - a_\alpha)/a_\alpha$, which can be calculated using the lattice parameters of the α and γ′ phases.

2.2. Gibbs energy of constituent phases

The Gibbs energy of the constituent phases was calculated using the CALPHAD database for Al–Fe–Mn–Ni system [27]. Fig. 2(a) shows the Gibbs-energy curves of the α, β, and γ phases at 300 K in the pseudo-binary system, calculated along the compositional line connecting the alloy (Fe–34Mn–15Al–7.5Ni) and β-phase (Fe–21.2Mn–29.4Al–34.0Ni) compositions. (Information regarding the β-phase composition was provided by Prof. T. Omori at Tohoku University (private communication, Jan. 20, 2024).) The horizontal axis in the figure represents the normalized composition c, and its correspondence with the composition of the Al–Fe–Mn–Ni quaternary system is listed in Table 1. $c = 1$ corresponds to the β-phase composition Fe–21.2Mn–29.4Al–34.0Ni, and $c = 0.221$ corresponds to the alloy composition Fe–34Mn–15Al–7.5Ni. $c = 0$ corresponds to the α-phase composition, where the Ni composition is assumed to be zero. Fig. 2(b) shows the Gibbs-energy curves of the constituent phases at 300 K, taking the common tangent to the Gibbs-energy curves of the β and γ phases as the energy reference. The Gibbs-energy values of the α and β phases are approximately the same at $c = 0$; therefore, the α + β two-phase state is assumed stable in equilibrium when the γ phase is absent. The Gibbs energy of the γ phase is lower than that of the α phase at $c = 0$, which can induce the MT from α to γ′. However, the Gibbs energy of the β phase is considerably lower than that of the γ phase at $c = 1$; therefore, the phase transformation

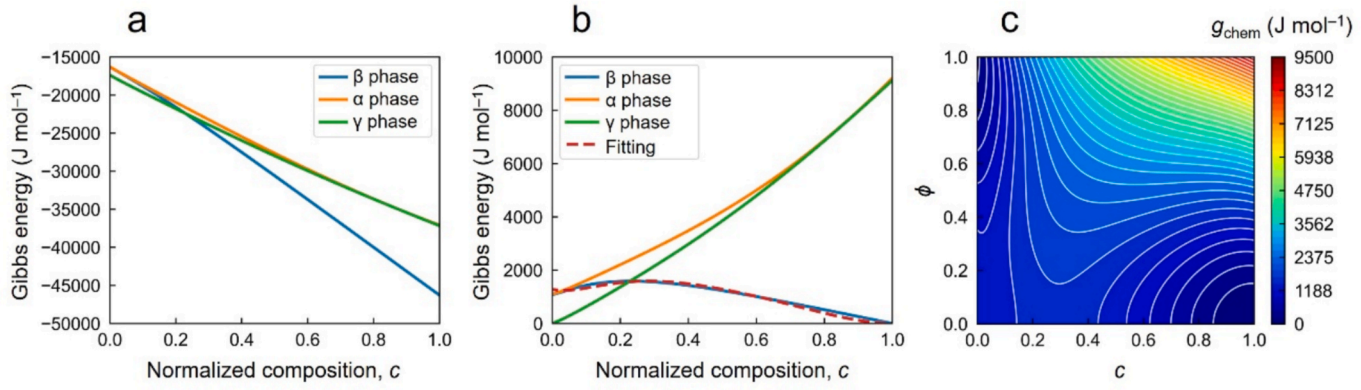

Fig. 2. (a) Gibbs-energy curves of the constituent phases calculated using the CALPHAD database for the Al–Fe–Mn–Ni system [27]. (b) Gibbs-energy curves of the constituent phases calculated by taking the common tangent to the Gibbs-energy curves of the β and γ phases as the energy reference. The red dashed line represents the chemical free-energy function (Eq. (5)) at $\phi_i = 0$ fitted to the Gibbs-energy curves of the α and β phases. (c) Contour plot of the chemical free energy in (c, ϕ) when a single OV domain of martensite is considered, i.e., $(\phi_1, \phi_2, \phi_3) = (\phi, 0, 0)$. (For interpretation of the references to colour in this figure legend, the reader is referred to the web version of this article.)

Table 1
Correspondence between the normalized composition c and composition of the Al–Fe–Mn–Ni quaternary system.

Normalized composition, c	Phase	Composition (at.%)			
		Fe	Mn	Al	Ni
0.0	α	bal.	37.6	10.9	0.0
0.221	–	bal.	34	15	7.5
1.0	β	bal.	21.2	29.4	34.0

from β to γ cannot easily occur.

The constants for the chemical free-energy function (Eq. (5)) were determined based on the Gibbs-energy curves shown in Fig. 2(b). The values of A_2, A_4, and A_8 were determined by fitting the chemical free-energy density function at $\phi_i = 0$ to the Gibbs-energy curves of the α and β phases. The red dashed line shown in Fig. 2(b) is the fitted curve, and the obtained values of A_2, A_4, and A_8 are 2.55×10^3, 5.28×10^4, and 7.24×10^4 J mol^{-1}, respectively. Considering a single OV domain $(\phi_1, \phi_2, \phi_3) = (\phi, 0, 0)$, the values of B_2, B_3, and B_4 were determined based on the following assumptions: (1) the chemical free-energy difference between the two states characterized by $(c, \phi) = (0, 1)$ and $(c, \phi) = (0, 0)$ is equal to the Gibbs-energy difference between the γ and α phase; (2) the chemical free-energy difference between the two states characterized by $(c, \phi) = (1, 1)$ and $(c, \phi) = (1, 0)$ is equal to the Gibbs-energy difference between the γ and β phases; and (3) $\partial g_{chem}/\partial \phi = 0$ is satisfied at $(c, \phi) = (0, 1)$. Based on these assumptions, the value of B_2 can be determined as $B_2 = -2.04 \times 10^4$ J mol^{-1}. Furthermore, if the value of c_+ is assumed, the values of B_3 and B_4 can be determined. In the present study, the values of $c_+ = -0.10$, $B_3 = 1.93 \times 10^4$ J mol^{-1}, and $B_4 = 1.73 \times 10^4$ J mol^{-1} were employed, which were determined so that the critical stress for the MT obtained from phase-field simulations under compressive loading would have approximately the same magnitudes as the experimentally measured values [12,16,31]. Fig. 2(c) shows the contour plot of the chemical free energy in (c, ϕ).

2.3. Simulation conditions

We performed three-dimensional (3D) simulations using 64 × 64 × 64 computational grids. Eqs. (1) and (2) were solved under the periodic boundary condition using the finite-difference method with the explicit Euler technique. In the numerical analysis, all physical parameters were reduced to dimensionless quantities using the following scaling factors: the product of the gas constant and absolute temperature RT for the energy; unit grid size in the finite-difference method l_0 for the length; and $(MRT/l_0^2)^{-1}$ or $(LRT)^{-1}$ for time.

First, the α + β microstructure was prepared by solving the temporal evolution of $c(\boldsymbol{r}, t)$ (Eq. (1)), during which the temporal evolution of $\phi_i(\boldsymbol{r}, t)$ (Eq. (2)) was not solved, and the value of ϕ_i was fixed at $\phi_i = 0$. To maintain numerical-calculation accuracy and stability, the unit time step was set to $\Delta t^* = 0.01 c_0(1 - c_0)$, where superscript * denotes a dimensionless quantity in numerical analysis, and c_0 represents the spatial average value of c. The simulation started from a single-phase state where the value of c fluctuated by ± 0.5% around the value of $c_0 = 0.221$, corresponding to the alloy composition (Fe–34Mn–15Al–7.5Ni). Subsequently, using the obtained α + β microstructure, the MT from α to γ′ under compressive loading was simulated by solving the temporal evolution of $\phi_i(\boldsymbol{r}, t)$ (Eq. (2)), during which the temporal evolution of $c(\boldsymbol{r}, t)$ (Eq. (1)) was not solved, i.e., the compositional field was fixed. Using the impurity diffusion coefficients in pure Fe at 300 K [32], the diffusion distances of Mn, Al, and Ni for 10^3 s are estimated as 2.3×10^{-21}, 3.9×10^{-22}, and 1.4×10^{-23} m, respectively, which justifies the assumption that the change in compositional field during the MT is negligibly small. The unit time step was set to $\Delta t^* = 0.05$ to maintain numerical-calculation accuracy and stability. The external compressive stress was applied in the $[100]_\alpha$ direction, where the transformation strain was maximized [18], and its magnitude was changed by 5 MPa every $100\Delta t^*$; it was first increased from 0 to 700 MPa and then decreased from 700 to 0 MPa, thereby simulating the MT and reverse MT during the loading and unloading of external stress, respectively. Other model parameters used in the simulations are listed in Table 2. (Information regarding the lattice parameter of the β phase was provided by Prof. T. Omori at Tohoku University (private communication, Jan. 20, 2024).)

Table 2
Model parameters used in the simulation.

Unit grid size (m)	$l_0 = 9.375 \times 10^{-10}$
Gradient-energy coefficient (J m^2 mol^{-1}) [33]	$\kappa_c = 5.0 \times 10^{-15}$
	$\kappa_\phi = 2.0 \times 10^{-15}$
Elastic modulus (GPa) [34]	$C_{11} = 154.5$
	$C_{12} = 118.0$
	$C_{44} = 105.2$
Lattice parameter (m) [12]	$a_\alpha = 2.903 \times 10^{-10}$
	$a_\beta = 2.908 \times 10^{-10}$
	$a_{\gamma'} = 3.672 \times 10^{-10}$

3. Results

3.1. α + β microstructure

To investigate the effect of the α + β microstructure on the SE properties of FMAN alloy, 3D phase-field simulations were first performed to obtain the α + β microstructures with different sizes and volume fractions of the β phase. Fig. 3 shows the results of a 3D phase-field simulation, illustrating the evolution of the α + β microstructure on a cross section. The alloy composition ($c_0 = 0.221$) is within the spinodal region where the Gibbs-energy curve has a negative curvature (see the red dashed line in Fig. 2(b)); therefore, the initial single phase with small composition fluctuations ($t^* = 0$) decomposes into Ni-poor ($0 \leqslant c \leqslant 0.5$) and Ni-rich ($0.5 < c \leqslant 1$) regions ($t^* = 3.4 - 10.3$), which are regarded as the α and β phases, respectively. Furthermore, the decomposed microstructure coarsens over time ($t^* = 13.8 - 20.7$); thus, we can obtain microstructures with almost the same volume fraction of the β phase but different average sizes of the β phase. Moreover, the α + β microstructure with different volume fractions of the β phase can be obtained through phase-field simulations by changing the alloy composition c_0. Table 3 summarizes the characteristics of the three types of microstructures prepared for the phase-field simulations of the MT from α to γ′ in Section 3.2. The average size of the β phase (d) is 10–16 nm, and the volume fraction of the β phase (V_f) is 17%–20%, both of which are close to the experimentally measured values [16,31].

3.2. Martensitic transformation from α to γ′ under compressive loading

A 3D phase-field simulation of the MT from α to γ′ under compressive loading in the $[100]_\alpha$ direction was performed using α + β microstructure #1 ($V_f = 19.6\%$, $d = 12.2$ nm) obtained in Section 3.1. Note that the compositional field c was fixed in the phase-field simulation of the MT. Fig. 4(a) shows the simulation results of the microstructure evolution during the loading ((i)–(iv)) and unloading ((iv)–(vii)) of external stress. The α phase is depicted as transparent, the β phase is shown in white, and OV1, OV2, and OV3 of the martensite (γ′) are shown in green, blue, and red, respectively. The region of $\phi_i > 0.55$ is assumed to correspond to the γ′ phase. During the loading of external stress, the MT from α to γ′ occurs, but no transformation occurs in the β phase. The γ′ phase has a structure composed of the OV2 and OV3 domains with a (011) twin boundary, enabling the effective relaxation of the internal elastic energy associated with the MT under uniaxial compressive stress along the $[100]_\alpha$ direction. During the unloading of the external stress, the reverse MT from γ′ to α occurs, finally completely reverting to the initial α + β microstructure before the external-stress loading. Fig. 4(b) shows the simulated stress–strain curve obtained by calculating the uniform macroscopic strain along the $[100]_\alpha$ direction. The critical stress for the MT is approximately 450 MPa, which is close to the experimentally measured value of 467 MPa for the Fe–30.5Mn–14.5Al–8Ni alloy ($V_f \sim 17\%$, $d \sim 12$ nm) [31]. Owing to the complete reverse MT from γ′ to α, the SE strain exceeds 6%, and the irrecoverable strain is zero.

Table 3
Characteristics of α + β microstructures obtained from phase-field simulations.

Microstructure	Composition, c_0	Volume fraction of β phase, V_f (%)	Average size of β phase, d (nm)
#1	0.221	19.6	12.2
#2	0.221	20.2	15.6
#3	0.200	17.0	10.5

Fig. 5(a) and (b) show the microstructure on a cross section under compressive stresses of 700 and 400 MPa, respectively, during the unloading of the external stress. Under an external stress of 700 MPa, a significant portion of the α phase transforms into the γ′ phase; however, a small amount of the α phase remains near the β-phase boundary and (011) twin boundary of the γ′ phase, as indicated by the arrows in Fig. 5 (a). As the magnitude of the external stress decreases from 700 MPa to 400 MPa, the size of the α phase increases, as indicated by the circles in Fig. 5(b), corresponding to the onset of the reverse MT from α to γ′.

The effect of the size and volume fraction of the β phase on the reversibility of the MT was investigated by altering the α + β microstructure used for the phase-field simulation of the MT. Fig. 6 shows the results of the phase-field simulation using α + β microstructure #2 ($V_f = 20.2\%$, $d = 15.6$ nm). Compared with microstructure #1, the size of the β phase is larger, but the volume fraction of the β phase does not change significantly. Fig. 6(a) shows the simulation results of microstructure evolution during the loading ((i)–(iii)) and unloading ((iii)–(iv)) of external compressive stress. During the loading of external stress, the MT from α to γ′ occurs and a martensite microstructure composed of the

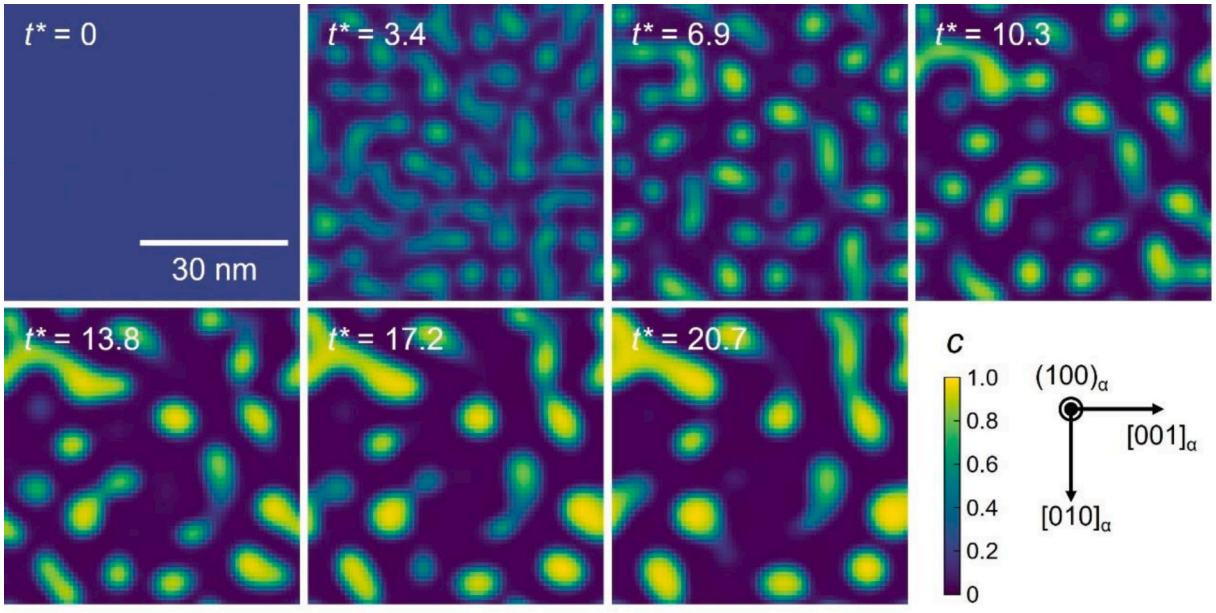

Fig. 3. Result of 3D phase-field simulation on Fe–34Mn–15Al–7.5Ni alloy, showing the evolution of the α + β microstructure on a cross section. The Ni-poor ($0 \leqslant c \leqslant 0.5$) and Ni-rich ($0.5 < c \leqslant 1$) regions are regarded as the α and β phases, respectively. t^* represents dimensionless time in numerical analysis.

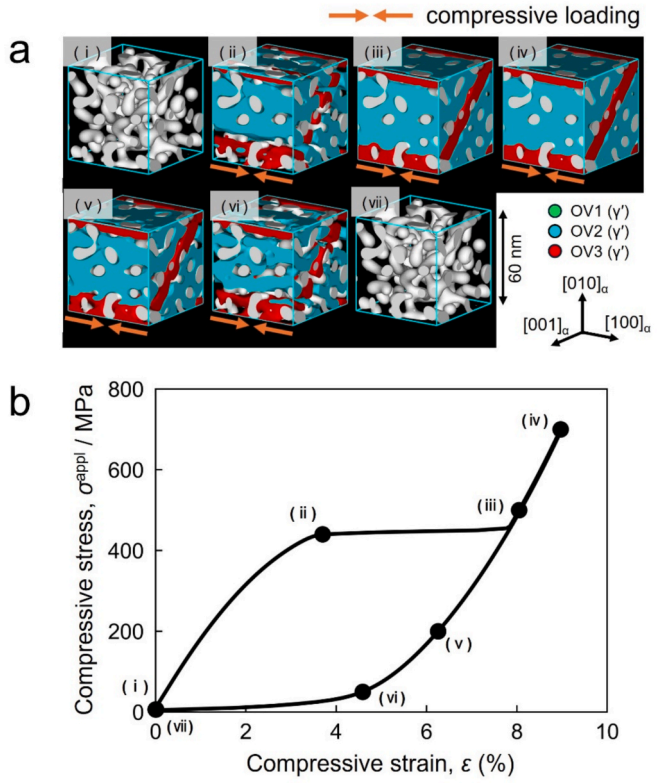

Fig. 4. Results of 3D phase-field simulation of MT from α to γ′ using α + β microstructure #1 ($V_f = 19.6\%$, $d = 12.2$ nm) under compressive loading in the $[100]_\alpha$ direction: (a) microstructure evolution and (b) corresponding stress–-strain curve. In (a), the α phase is depicted as transparent, the β phase is shown in white, and the three OVs (OV1, OV2, and OV3) of the γ′ phase are shown in green, blue, and red, respectively. (For interpretation of the references to colour in this figure legend, the reader is referred to the web version of this article.)

OV2 and OV3 domains with a (011) twin boundary is formed, as in the case of microstructure #1 (Fig. 4). However, during the unloading of external stress, only a slight reverse MT from γ′ to α occurs, and a considerable amount of retained γ′ is observed in the microstructure after the external stress is removed ((iv)). Fig. 6(b) shows the corresponding stress–strain curve obtained from the simulation. The critical stress for the MT is approximately 100 MPa lower than that for microstructure #1. Furthermore, the reverse MT hardly occurs; thus, the SE strain is less than 1%, and the irrecoverable strain is approximately 5%.

Similarly, the phase-field simulation of the MT was performed using α + β microstructure #3 ($V_f = 17.0\%$, $d = 10.5$ nm). The size and volume fraction of the β phase are smaller than those of microstructure #1. Fig. 7 (a) shows the simulation results of the microstructure evolution during the loading ((i)–(iii)) and unloading ((iii)–(iv)) of the external compressive stress. As in the cases of microstructures #1 and #2 (Figs. 4 and 6), the MT from α to γ′ is induced by the compressive stress, resulting in a martensite microstructure composed of the OV2 and OV3 domains with a (011) twin boundary. However, only a slight reverse MT from γ′ to α occurs during the unloading of the external stress, as in the case of microstructure #2 (Fig. 6). The corresponding stress–strain curve (Fig. 7 (b)) demonstrates that the critical stress for the MT is slightly lower than that for microstructure #1, the SE strain is less than 1%, and the irrecoverable strain exceeds 5%.

4. Discussion

4.1. Reversibility of MT and free-energy change

The results shown in Figs. 4, 6, and 7 indicate that the reversibility of the MT varies depending on the size and volume fraction of the β phase, which has also been demonstrated through experiments [16,25,31]. Herein, we consider interpreting this phenomenon from the perspective of the free-energy change during the MT and reverse MT. Fig. 8(a) and (b) show the changes in the chemical free-energy field (g_{chem}) and elastic-energy field (e_{el}), respectively, on the cross section corresponding to Fig. 5 during the loading (0 → 460 → 700 MPa) and unloading (700 → 400 → 200 MPa) of the external stress. Note that in Fig. 8, the energy field before the external-stress loading is taken as the energy reference. As shown in Figs. 4 and 5, the γ′ phase, which has a structure composed of OV2 and OV3, coexists with the β phase when the magnitude of the external stress sequentially changes from 460 to 700, 400, and 200 MPa. The elastic energy of the β phase increases ($\Delta e_{el} > 0$) owing to the MT of the surrounding α phase, and the magnitude of Δe_{el} increases as the external-stress magnitude increases (Fig. 8(b)). Moreover, a comparison of Fig. 8(a) and (b) shows that the chemical free energy increases ($\Delta g_{chem} > 0$) in the β phase, where $\Delta e_{el} > 0$. More specifically, the β phase located within the OV domain of the γ′ phase has larger and positive values of Δe_{el} and Δg_{chem}, whereas the β phase at the OV interface (twin boundary) of the γ′ phase has smaller and positive values of Δe_{el} and Δg_{chem} (see the arrows in Fig. 8(a) and (b)).

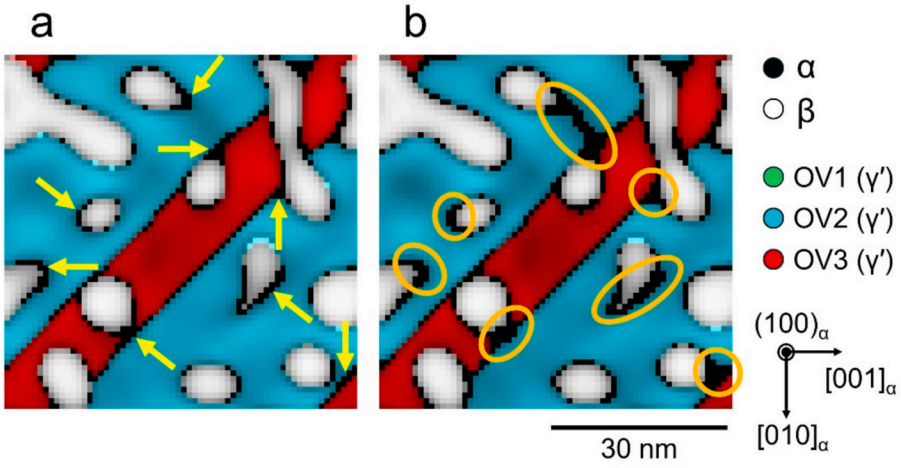

Fig. 5. Microstructure on a cross section under the external compressive stress of (a) 700 MPa and (b) 400 MPa during the unloading of the external stress. The α phase is shown in black, the β phase is shown in white, and the three OVs (OV1, OV2, and OV3) of the γ′ phase are shown in green, blue, and red, respectively. (For interpretation of the references to colour in this figure legend, the reader is referred to the web version of this article.)

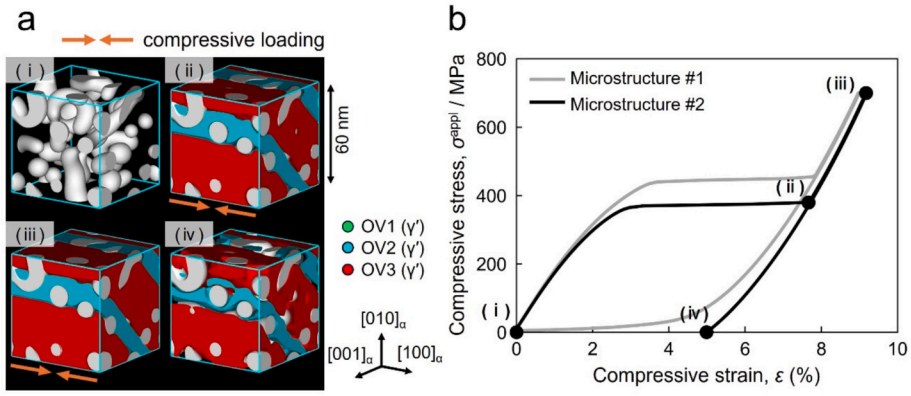

Fig. 6. Results of 3D phase-field simulation of the MT from α to γ′ using α + β microstructure #2 ($V_f = 20.2\%$, $d = 15.6$ nm) under compressive loading in the $[100]_\alpha$ direction: (a) microstructure evolution and (b) corresponding stress–strain curve. In (a), the α phase is depicted as transparent, the β phase is shown in white, and the three OVs (OV1, OV2, and OV3) of the γ′ phase are shown in green, blue, and red, respectively. (For interpretation of the references to colour in this figure legend, the reader is referred to the web version of this article.)

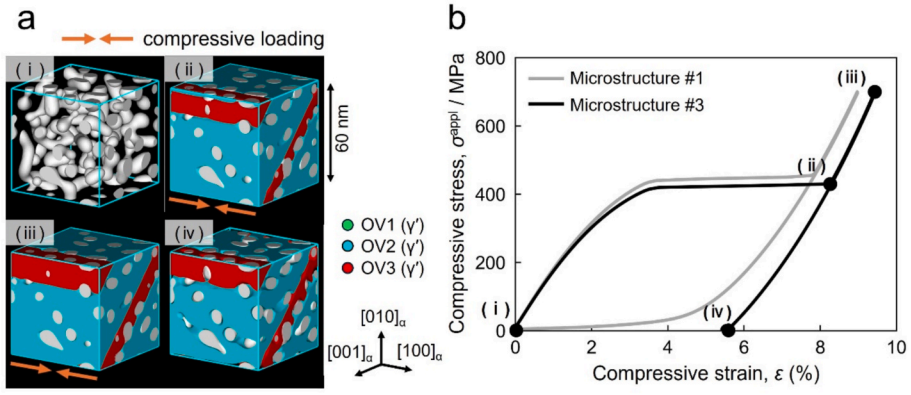

Fig. 7. Results of 3D phase-field simulation of the MT from α to γ′ using α + β microstructure #3 ($V_f = 17.0\%$, $d = 10.5$ nm) under compressive loading in the $[100]_\alpha$ direction: (a) microstructure evolution and (b) corresponding stress–strain curve. In (a), the α phase is depicted as transparent, the β phase is shown in white, and the three OVs (OV1, OV2, and OV3) of the γ′ phase are shown in green, blue, and red, respectively. (For interpretation of the references to colour in this figure legend, the reader is referred to the web version of this article.)

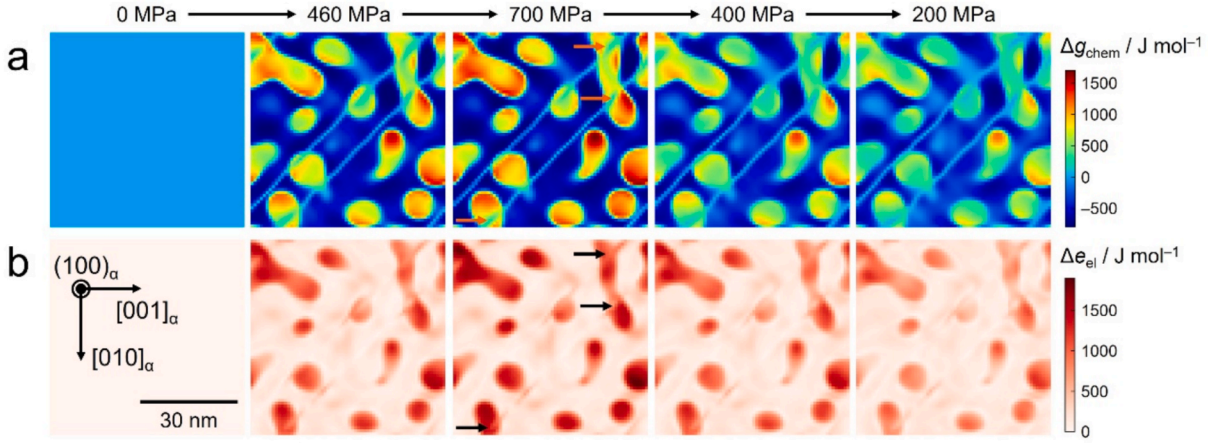

Fig. 8. Changes in free-energy fields on the cross section corresponding to Fig. 5 during the loading (0 → 460 → 700 MPa) and unloading (700 → 400 → 200 MPa) of the external stress: (a) chemical free-energy field and (b) elastic-energy field.

A cross section of the γ′ + β microstructure under a compressive-stress loading of 700 MPa, along with the corresponding fields of ϕ_2, Δg_{chem}, and Δe_{el}, are shown in Fig. 9(a, b), (c), (d), and (e), respectively. The β-phase regions ($0.5 < c \leqslant 1$) are outlined with dashed lines in Fig. 9 (c), (d), and (e). The β phase is stable because its Gibbs energy is considerably lower compared with that of the γ phase (see Fig. 2). However, the elastic energy within the β phase acts as the driving force for the phase transformation; therefore, the value of ϕ_2 (the structural

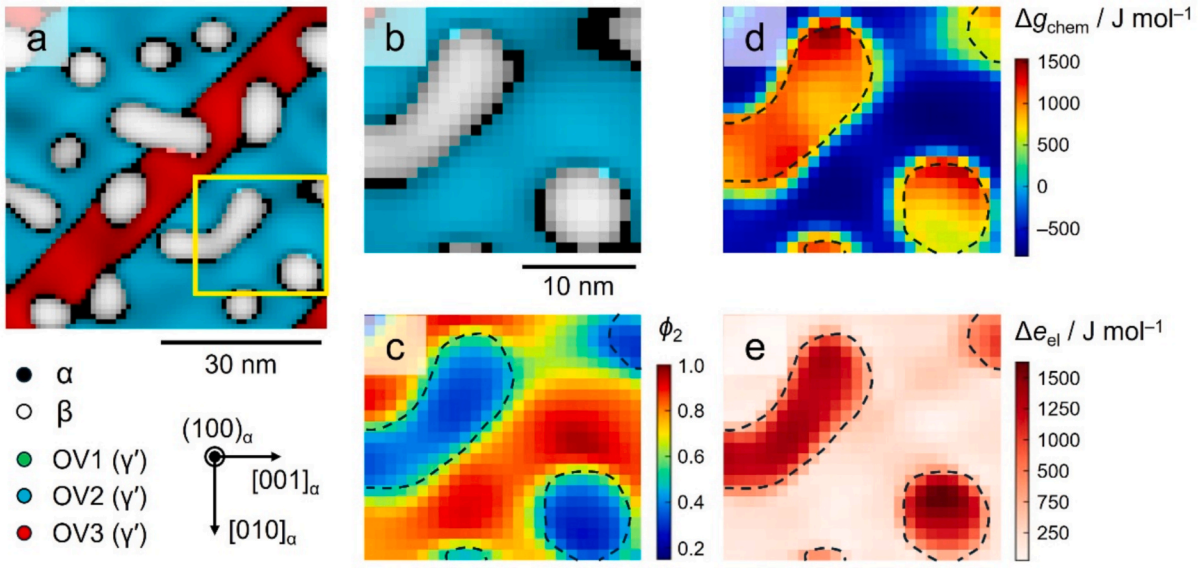

Fig. 9. Relationship between microstructure and changes in energy fields on a cross section under the compressive stress of 700 MPa. (a) γ′ + β microstructure and (b) enlarged view of the microstructure enclosed by the rectangle in (a). (c), (d), and (e) are the fields of ϕ_2, Δg_{chem}, and Δe_{el} on the cross section corresponding to (b), respectively.

density of OV2) slightly increases in the β phase (Fig. 9(c)). As a result, the value of g_{chem} also increases (Fig. 9(d)). Notably, near the β-phase boundary, the value of g_{chem} increases while the value of ϕ_2 decreases in the γ′ phase (Fig. 9(c)). This indicates that near the β-phase boundary, the γ′ phase is destabilized or the untransformed α phase is present. This is because the compositional gradient that occurs near the β-phase boundary suppresses the MT from α to γ′ (see also the chemical free-energy landscape in Fig. 2(c)). Figs. 8 and 9 show the results when the external compressive stress is applied to microstructure #1; however, similar results are obtained when the external compressive stress is applied to microstructures #2 and #3 as well.

Fig. 10(a) shows the change in the total free energy G_{sys} in microstructure #1 during the loading and unloading of the external stress, along with the changes in G_{chem}, E_{grad}, E_{el}, and E_{pot}. In the initial stage of external-stress loading, when the external stress is below the critical stress for the MT, G_{chem} increases owing to the energy barrier for the MT from α to γ′. When the external stress exceeds the critical stress for the MT, the MT from α to γ′ occurs, which significantly reduces G_{chem} and causes ΔG_{chem} to become negative. Thereafter, as the external stress increases, G_{chem} slightly increases, which corresponds to the destabilization of the β phase owing to internal elastic energy (the increase in the values of e_{el} and ϕ_2 in the β phase), as shown in Figs. 8 and 9. Subsequently, during the unloading of the external stress, G_{chem} decreases slightly with the external stress. When the reverse MT from γ′ to α begins, G_{chem} increases, and when the reverse MT is complete, ΔG_{chem} eventually becomes zero. E_{el} significantly increases when the MT from α to γ′ occurs, and then gradually increases as the external-stress magnitude increases. This is caused by the elastic energy stored within the β phase (see Figs. 8 and 9). However, the MT from α to γ′ results in a large negative value of E_{pot}; therefore, G_{sys} takes a negative value from the beginning of the external-stress loading and its magnitude increases with the external stress. Furthermore, during the unloading of the external stress, E_{el} decreases with the external stress. The reverse MT from γ′ to α causes a further decrease in E_{el}, and ΔE_{el} eventually becomes zero when the reverse MT is complete. E_{grad} increases during the MT from α to γ′ and decreases during the reverse MT from γ′ to α; however, these changes are insignificant compared with those in G_{chem} and E_{el}.

Fig. 10(b) and (c) show the changes in free energy during the loading and unloading of the external stress for microstructures #2 and #3, respectively. The behavior of the free-energy change is similar to that for microstructure #1. However, unlike in the case of microstructure #1, a considerable amount of γ′ remains without undergoing the reverse transformation to α even after the external stress is removed (see Figs. 6 and 7); thus, ΔG_{chem} and ΔE_{el} have negative and positive values, respectively. A common feature of microstructures #1, #2, and #3 is that ΔG_{sys} becomes zero when the external stress is removed. In microstructure #1, ΔG_{sys} temporarily shows positive values during the unloading of the external stress, which leads to the reverse MT from γ′ to α, thereby reducing G_{sys}; when the external stress is removed, ΔG_{sys} becomes zero. In contrast, in microstructures #2 and #3, where the reverse MT from γ′ to α hardly occurs, ΔG_{sys} remains negative throughout the loading and unloading of the external stress and becomes zero when the external stress is removed. These results suggest that the state with $\Delta G_{sys} > 0$ during the unloading of the external stress creates a pathway for the complete reverse MT from γ′ to α; thus, the SE strain exceeds 6%.

The reversibility of MT, that is, the sign of ΔG_{sys} during the unloading of the external stress, is influenced by the magnitudes of both ΔG_{chem} and ΔE_{el}. However, in the cases of microstructures #1, #2, and #3, this is mainly determined by the magnitude of ΔG_{chem}. Fig. 10 shows that the decrease in G_{chem} caused by the MT from α to γ′ in microstructure #1 is smaller compared to that in microstructures #2 and #3. Fig. 11(a) shows the histograms of Δg_{chem} in microstructures #1, #2, and #3 under an external compressive stress of 700 MPa. Furthermore, Fig. 11(b) compares the total increase and decrease in g_{chem} in each of the three microstructures. As shown in Fig. 9, Δg_{chem} generally has positive values within the β phase and negative values within the γ′ phase. As shown in Fig. 11(a), the frequency of the β-phase regions with large positive values of Δg_{chem} is higher in microstructure #3 than in microstructures #1 and #2. However, the volume fraction of the β phase is lower in microstructure #3 than in microstructures #1 and #2 (see Table 3); therefore, the total increase in g_{chem} is approximately the same between the three microstructures, as shown in Fig. 11(b). However, the frequency of the γ′-phase regions with large negative values of Δg_{chem} is higher in microstructures #2 and #3 than in microstructure #1 (Fig. 11 (a)); therefore, the total decrease in g_{chem} is also greater in microstructures #2 and #3 than in microstructure #1 (Fig. 11(b)). As shown in Fig. 9, g_{chem} increases in the γ′ phase near the β-phase boundary,

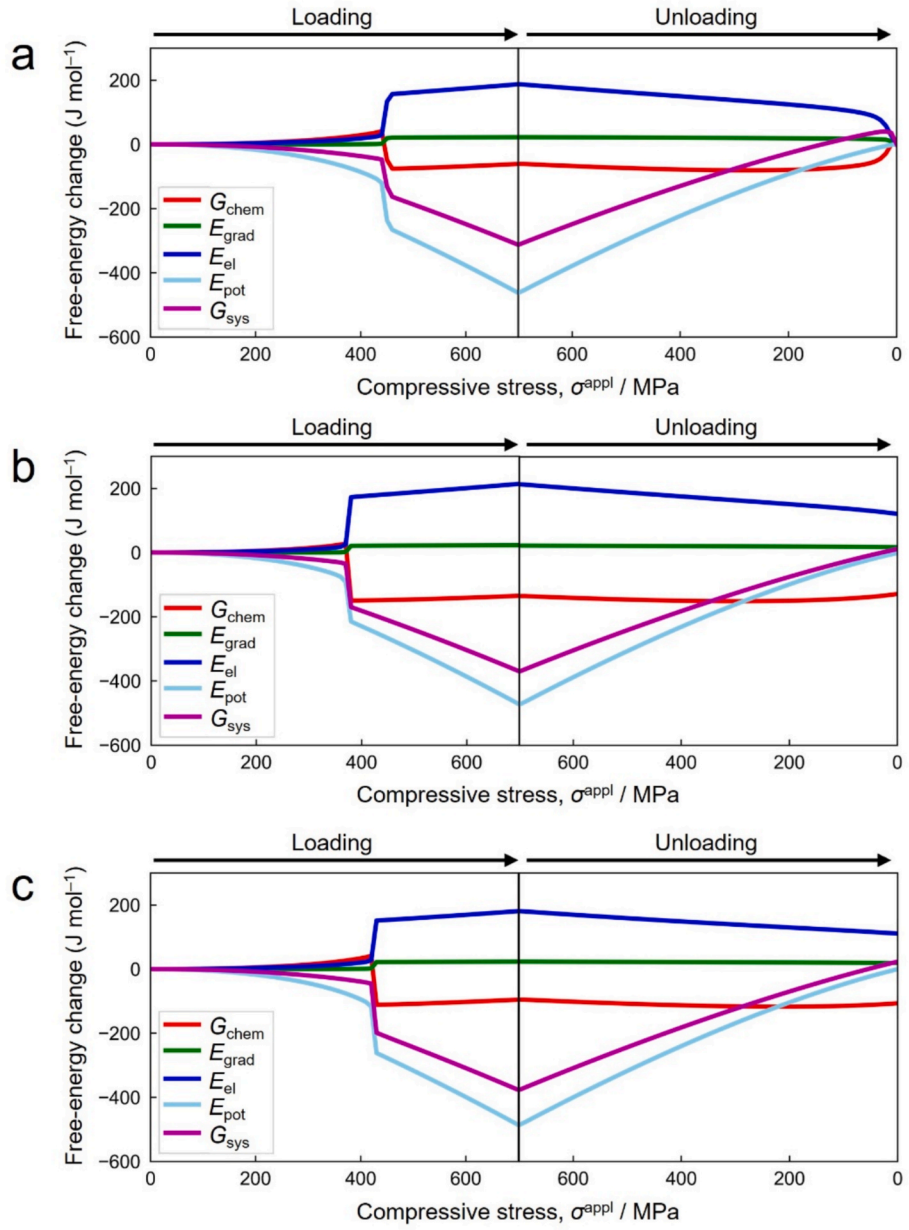

Fig. 10. Change in the total free energy G_{sys} during the loading and unloading of external stress, along with the changes in G_{chem}, E_{grad}, E_{el}, and E_{pot}: (a) microstructure #1, (b) microstructure #2, and (c) microstructure #3.

indicating that the total decrease in g_{chem} becomes greater if the volume fraction of the β phase decreases and/or the size of the β phase increases, thereby reducing the β-phase boundary region. This is the reason for the greater total decrease in g_{chem} in microstructures #2 and #3 than in microstructure #1. As a result, ΔG_{sys} remains negative during the unloading of the external stress in microstructures #2 and #3, preventing the reverse MT from γ′ to α. These results suggest that the reversibility of MT can be explained in terms of the sign of the total free-energy change, i.e., the balance between ΔG_{chem} and ΔE_{el}, during the unloading of the external stress, and controlling the size and volume fraction of the β phase enables the regulation of the SE strain of the FMAN alloy.

4.2. Limitations

The value of parameter c_+ for the chemical free energy was determined such that the critical stress for the MT obtained from the simulation would be approximately the same magnitude as the experimentally measured values [12,16,31]. On the other hand, the simulated stress–strain curves for microstructures #1 and #2 (Fig. 4(b) and 6(b)) indicate that the critical stress for the MT decreases as the size of the β phase (d) increases. This result may seem to contradict the trend reported in the experimental study [16], where the d-dependence of the SE properties of FMAN alloy was clarified by changing the α + β microstructure through aging heat treatments. However, it should be noted that in the experiment, not only d but also the volume fraction of the β phase (V_f) changes during aging [16], whereas V_f is almost the same between the microstructures #1 and #2 in our simulation. The SE properties of FMAN alloy (including the critical stress for the MT and the SE strain) are influenced by V_f, d, and the chemical composition of the β phase [16,25,31], among which V_f has a non-negligible effect [31]. It has been reported that optimal SE properties of FMAN alloy are obtained when d = 6–10 nm [16]. However, the simulated SE strain for microstructure #3 (V_f = 17.0%, d = 10.5 nm) was less than 1% (Fig. 7). This

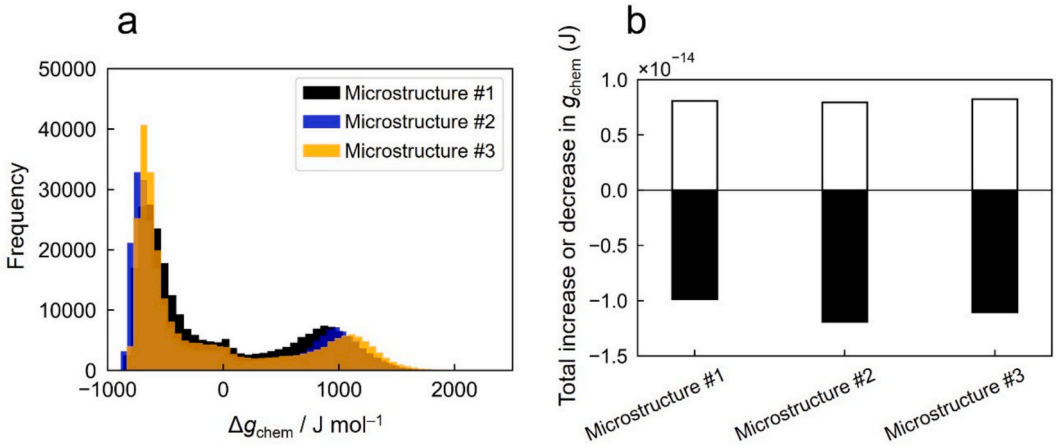

Fig. 11. Change in chemical free energy caused by the MT from α to γ′ under the external compressive stress of 700 MPa: (a) histograms of Δg_{chem} in microstructures #1, #2, and #3, and (b) comparison of total increase and decrease in g_{chem} in microstructures #1, #2, and #3.

discrepancy is likely due to the difference in V_f between the experiment and the simulation. The results in Section 4.1 indicate that even if d is optimized to 6–10 nm, the reverse MT from γ′ to α is unlikely to occur when the value of V_f is small. Therefore, to comprehensively understand the relationship between the α + β microstructure and the SE properties of FMAN alloy, further experimental and simulation studies that systematically vary both V_f and d will be necessary. Meanwhile, the use of the pseudo-binary Gibbs-energy curves of the constituent phases in the phase-field model may make it difficult to reproduce the partitioning behavior of solute elements between the α and β phases during aging [16,31] and to discuss its effects on the SE properties of FMAN alloy. Furthermore, because the simulation domain size is small (60 × 60 × 60 nm^3), the stress–strain curves obtained from the simulations may not necessarily correspond to the macroscopic stress–strain curves obtained from experiments. Therefore, in the future, it will also be necessary to enlarge the simulation domain size in order to quantitatively compare the simulation and experimental results.

Our simulations did not consider the loss of coherency between the β and matrix phases, nor the plastic deformation during the MT, but these have been reported to degrade the SE properties of FMAN alloy [14,16,20]; both of them would reduce the internal elastic energy (E_{el}), thus altering the balance between ΔG_{chem} and ΔE_{el}, and making the reverse MT from γ′ to α less likely to occur. To investigate the effect of plasticity on the SE properties of FMAN alloy, it is necessary to develop an advanced phase-field model that takes into account the plastic deformation during the MT, as reported in simulation studies on the MT in low-carbon steel [35,36]. Moreover, the MT from α to γ′ may be accompanied by the structural change of the β phase from B2 to $L1_0$, generating additional elastic energy in the β phase [37,38]. During the MT from α to γ′, the elastic energy stored in the β phase (see Fig. 8 and 9 (e)) may cause the structural transformation from B2 to $L1_0$, which is an issue to be addressed in the future.

Owing to the lack of experimental data on the elastic modulus of the constituent phases, an elastically homogeneous system was assumed in our simulation. If the degree of the elastic inhomogeneity (e.g., the difference in elastic modulus between the α and β phases) is large, the magnitude of the elastic energy stored in the β phase will change, resulting in a change in the balance between ΔG_{chem} and ΔE_{el}. Detailed information on parameters such as the lattice parameters and elastic moduli (including their temperature dependences) of the phase-field model is extremely important for predicting and controlling the SE properties of FMAN alloy, and should be clarified in the future.

5. Conclusions

We conducted 3D phase-field simulations of the MT from α to γ′ and reverse MT from γ′ to α during the loading and unloading of external compressive stress along the $[100]_\alpha$ direction to investigate the effects of the size (d) and volume fraction (V_f) of nanoscale β phase in the α phase on the SE strain (reversibility of MT) in Fe–Mn–Al–Ni alloy. The findings obtained are as follows.

1. The MT from α to γ′ was induced by the external compressive stress of approximately 400 MPa, resulting in a martensite microstructure composed of the OV2 and OV3 domains with a (011) twin boundary. No transformation occurred in the β phase because its Gibbs energy was significantly lower compared to the γ phase. A small amount of the α phase remained near the β-phase boundary and (011) twin boundary of the γ′ phase.
2. During the unloading of the external stress, the size of the α phase increased near the β-phase boundary and (011) twin boundary of the γ′ phase, corresponding to the onset of the reverse MT from γ′ to α. When the external stress was removed, the reverse MT was completed in microstructure #1 ($V_f = 19.6\%$, $d = 12.2$ nm), reverting to the initial α + β microstructure before the external stress loading, resulting in an SE strain exceeding 6%. However, in microstructures #2 ($V_f = 20.2\%$, $d = 15.6$ nm) and #3 ($V_f = 17.0\%$, $d = 10.5$ nm), only a slight reverse MT occurred, and the SE strain remained below 1%.
3. The MT of the α phase increased the elastic energy of the β phase, which acted as the driving force for the phase transformation and destabilized the β phase. As a result, the structural density of martensite in the β phase slightly increased, which, in turn, increased the chemical free energy of the β phase. Furthermore, compositional gradient near the β-phase boundary suppressed the MT from α to γ′, decreased the structural density of martensite, and thereby increased the chemical free energy of the γ′ phase.
4. A complete reverse MT occurred in microstructure #1 when the total free-energy change temporarily became positive during the unloading of the external stress. This indicates that the reversibility of the MT can be explained in terms of the sign of the total free-energy change, i.e., the balance between the elastic-energy change and chemical free-energy change, under external stress loading. This study has demonstrated that during the MT from α to γ′, an increase in the chemical free energy of the γ′ phase near the β-phase boundary significantly affects the total free-energy change, which explains why the SE strain varies depending on the size and volume fraction of the β phase.

CRediT authorship contribution statement

Miyu Takagi: Writing – original draft, Visualization, Software, Methodology. **Yuhki Tsukada:** Writing – review & editing, Supervision, Methodology, Funding acquisition, Conceptualization. **Toshiyuki Koyama:** Writing – review & editing. **Dasom Kim:** Writing – review & editing. **Naoki Takata:** Writing – review & editing.

Funding

This work was supported by JSPS KAKENHI Grant Numbers JP23H00231, JP26K01242.

Declaration of competing interest

The authors declare that they have no known competing financial interests or personal relationships that could have appeared to influence the work reported in this paper.

Acknowledgments

The authors thank Prof. T. Omori (Tohoku University, Japan) and Prof. H. Akamine (Nagasaki University, Japan) for fruitful discussions on the reversibility of martensitic transformation in Fe–Mn–Al–Ni alloy.

Data availability

Data will be made available on request.

References

[1] J.M. Jani, M. Leary, A. Subic, M.A. Gibson, A review of shape memory alloy research, applications and opportunities, Mater. Des. 56 (2014) 1078–1113, https://doi.org/10.1016/j.matdes.2013.11.084.
[2] R. Kainuma, Recent progress in shape memory alloys, Mater. Trans. 59 (2018) 327–331, https://doi.org/10.2320/matertrans.M2017340.
[3] A. Sato, E. Chishima, K. Soma, T. Mori, Shape memory effect in γ⇄ϵ transformation in Fe-30Mn-1Si alloy single crystals, Acta Metall. 30 (1982) 1177–1183, https://doi.org/10.1016/0001-6160(82)90011-6.
[4] T. Sawaguchi, T. Maruyama, H. Otsuka, A. Kushibe, Y. Inoue, K. Tsuzaki, Design concept and applications of Fe–Mn–Si-based alloys—from shape-memory to seismic response control, Mater. Trans. 57 (2016) 283–293, https://doi.org/10.2320/matertrans.MB201510.
[5] T. Maki, K. Kobayashi, M. Minato, I. Tamura, Thermoelastic martensite in an ausaged Fe-Ni-Ti-Co alloy, Scr. Metall. 18 (1984) 1105–1109, https://doi.org/10.1016/0036-9748(84)90187-X.
[6] Y. Tanaka, Y. Himuro, R. Kainuma, Y. Sutou, T. Omori, K. Ishida, Ferrous polycrystalline shape-memory alloy showing huge superelasticity, Science 327 (2010) 1488–1490, https://doi.org/10.1126/science.1183169.
[7] Y. Sohail, C. Zhang, D. Xue, J. Zhang, D. Zhang, S. Gao, Y. Yang, X. Fan, H. Zhang, G. Liu, J. Sun, E. Ma, Machine-learning design of ductile FeNiCoAlTa alloys with high strength, Nature 643 (2025) 119–124, https://doi.org/10.1038/s41586-025-09160-2.
[8] D. Lee, T. Omori, R. Kainuma, Ductility enhancement and superelasticity in Fe–Ni–Co–Al–Ti–B polycrystalline alloy, J. Alloys Compd. 617 (2014) 120–123, https://doi.org/10.1016/j.jallcom.2014.07.136.
[9] J. Cassinerio, M.F. Giordana, E. Zelaya, V. Remich, P. Krooß, J. Freudenberger, T. Niendorf, C.E. Sobrero, On the impact of γ́ precipitates on the transformation temperatures in Fe–Ni–Co–Al–Ti–B shape memory alloy wires, Shape Mem. Superelasticity 10 (2024) 37–44, https://doi.org/10.1007/s40830-023-00470-w.
[10] V. Remich, C. Lauhoff, M.J. Kriegel, M. Motylenko, T. Niendorf, P. Krooß, On the effect of chemical heterogeneity on the shape memory performance of Fe–Ni–Co–Al–Ti single crystals, Shape Mem. Superelasticity 10 (2024) 452–459, https://doi.org/10.1007/s40830-024-00511-y.
[11] S. Xu, T. Omori, R. Kainuma, Superelasticity in micro-sized Fe–Ni–Co–Al–Ti–B shape memory alloys, Shape Mem. Superelasticity 12 (2026) 223–228, https://doi.org/10.1007/s40830-026-00600-0.
[12] T. Omori, K. Ando, M. Okano, X. Xu, Y. Tanaka, I. Ohnuma, R. Kainuma, K. Ishida, Superelastic effect in polycrystalline ferrous alloys, Science 333 (2011) 68–71, https://doi.org/10.1126/science.1202232.
[13] K. Ando, T. Omori, I. Ohnuma, R. Kainuma, K. Ishida, Ferromagnetic to weak-magnetic transition accompanied by bcc to fcc transformation in Fe–Mn–Al alloy, Appl. Phys. Lett. 95 (2009) 212504, https://doi.org/10.1063/1.3266848.
[14] L.W. Tseng, J. Ma, S.J. Wang, I. Karaman, M. Kaya, Z.P. Luo, Y.I. Chumlyakov, Superelastic response of a single crystalline FeMnAlNi shape memory alloy under tension and compression, Acta Mater. 89 (2015) 374–383, https://doi.org/10.1016/j.actamat.2015.01.009.
[15] T. Omori, R. Kainuma, Martensitic transformation and superelasticity in Fe–Mn–Al-based shape memory alloys, Shape Mem. Superelasticity 3 (2017) 322–334, https://doi.org/10.1007/s40830-017-0129-9.
[16] L.W. Tseng, J. Ma, B.C. Hornbuckle, I. Karaman, G.B. Thompson, Z.P. Luo, Y. I. Chumlyakov, The effect of precipitates on the superelastic response of [100] oriented FeMnAlNi single crystals under compression, Acta Mater. 97 (2015) 234–244, https://doi.org/10.1016/j.actamat.2015.06.061.
[17] L. Janke, C. Czaderski, M. Motavalli, J. Ruth, Applications of shape memory alloys in civil engineering structures—Overview, limits and new ideas, Mat. Struct. 38 (2005) 578–592, https://doi.org/10.1007/BF02479550.
[18] L.W. Tseng, J. Ma, Y.I. Chumlyakov, I. Karaman, Orientation dependence of superelasticity in FeMnAlNi single crystals under compression, Scr. Mater. 166 (2019) 48–52, https://doi.org/10.1016/j.scriptamat.2019.02.034.
[19] A. Bauer, M. Vollmer, T. Niendorf, Effect of crystallographic orientation and grain boundaries on martensitic transformation and superelastic response of oligocrystalline Fe–Mn–Al–Ni shape memory alloys, Shape Mem. Superelasticity 7 (2021) 373–382, https://doi.org/10.1007/s40830-021-00340-3.
[20] R. Lehnert, M. Müller, M. Vollmer, P. Krooß, G. Korpala, U. Prahl, M. Wendler, O. Volkova, T. Niendorf, H. Biermann, A. Weidner, On the influence of crystallographic orientation on superelasticity - Fe-Mn-Al-Ni shape memory alloys studied by advanced in situ characterization techniques, Mater. Sci. Eng. A-Struct. Mater. Prop. Microstruct. Process. 871 (2023) 144830, https://doi.org/10.1016/j.msea.2023.144830.
[21] H. Sehitoglu, I. Karaman, X.Y. Zhang, Y. Chumlyakov, H.J. Maier, Deformation of FeNiCoTi shape memory single crystals, Scr. Mater. 44 (2001) 779–784, https://doi.org/10.1016/S1359-6462(00)00657-6.
[22] H. Sehitoglu, X.Y. Zhang, T. Kotil, D. Canadinc, Y. Chumlyakov, H.J. Maier, Shape memory behavior of FeNiCoTi single and polycrystals, Metall. Mater. Trans. A 33 (2002) 3661–3672, https://doi.org/10.1007/s11661-002-0240-0.
[23] H. Sehitoglu, C. Efstathiou, H.J. Maier, Y. Chumlyakov, Hysteresis and deformation mechanisms of transforming FeNiCoTi, Mech. Mater. 38 (2006) 538–550, https://doi.org/10.1016/j.mechmat.2005.05.024.
[24] J. Ma, B.C. Hornbuckle, I. Karaman, G.B. Thompson, Z.P. Luo, Y.I. Chumlyakov, The effect of nanoprecipitates on the superelastic properties of FeNiCoAlTa shape memory alloy single crystals, Acta Mater. 61 (2013) 3445–3455, https://doi.org/10.1016/j.actamat.2013.02.036.
[25] P. La Roca, A. Baruj, C.E. Sobrero, J.A. Malarría, M. Sade, Nanoprecipitation effects on phase stability of Fe-Mn-Al-Ni alloys, J. Alloys Compd. 708 (2017) 422–427, https://doi.org/10.1016/j.jallcom.2017.02.280.
[26] T. Omori, M. Nagasako, M. Okano, K. Endo, R. Kainuma, Microstructure and martensitic transformation in the Fe-Mn-Al-Ni shape memory alloy with B2-type coherent fine particles, Appl. Phys. Lett. 101 (2012) 231907, https://doi.org/10.1063/1.4769375.
[27] A. Walnsch, M.J. Kriegel, O. Fabrichnaya, A. Leineweber, Thermodynamic assessment and experimental investigation of the systems Al–Fe–Mn and Al–Fe–Mn–Ni, Calphad 66 (2019) 101621, https://doi.org/10.1016/j.calphad.2019.04.006.
[28] L.-Q. Chen, Phase-field models for microstructure evolution, Annu. Rev. Mater. Res. 32 (2002) 113–140, https://doi.org/10.1146/annurev.matsci.32.112001.132041.
[29] Y. Ni, Y.M. Jin, A.G. Khachaturyan, The transformation sequences in the cubic → tetragonal decomposition, Acta Mater. 55 (2007) 4903–4914, https://doi.org/10.1016/j.actamat.2007.05.016.
[30] A.G. Khachaturyan, Theory of Structural Transformations in Solids, Dover, New York, 2008.
[31] A. Walnsch, A. Bauer, J. Freudenberger, K. Freiberg, C. Wüstefeld, M. Vollmer, S. Lippmann, T. Niendorf, A. Leineweber, M.J. Kriegel, Thermodynamically guided improvement of Fe–Mn–Al–Ni shape-memory alloys, Adv. Mater. 36 (2024) 2306794, https://doi.org/10.1002/adma.202306794.
[32] The Japan Institute of Metals and Materials, Metals data book, 3rd ed., Maruzen, Tokyo, 1993.
[33] T. Koyama, K. Hashimoto, H. Onodera, Phase-field simulation of phase transformation in Fe-Cu-Mn-Ni quaternary alloy, Mater. Trans. 47 (2006) 2765–2772, https://doi.org/10.2320/matertrans.47.2765.
[34] S. Mikami, A. Nagakubo, Y. Ohara, J. Xia, T. Omori, Measurement of elastic constants of single-crystal iron-based superelastic alloy using resonant ultrasound spectroscopy with a laser Doppler interferometer, in: Proceedings of the 33rd Symposium on Non-Destructive Inspection, The Japanese Society for Non-Destructive Inspection, Tokyo, 2026, pp. 33–34.
[35] Y. Tsukada, Y. Kojima, T. Koyama, Y. Murata, Phase-field simulation of habit plane formation during martensitic transformation in low-carbon steels, ISIJ Int. 55 (2015) 2455–2462, https://doi.org/10.2355/isijinternational.ISIJINT-2015-039.
[36] Y. Tsukada, A. Yoshida, R. Yamazaki, T. Koyama, Phase-field simulation of distribution of dislocation density and internal stress in as-quenched martensite in low-carbon steel, Comput. Mater. Sci. 259 (2025) 114171, https://doi.org/10.1016/j.commatsci.2025.114171.
[37] A. Walnsch, M.J. Kriegel, M. Motylenko, G. Korpala, U. Prahl, A. Leineweber, Thermodynamics of martensite formation in Fe–Mn–Al–Ni shape memory alloys, Scr. Mater. 192 (2021) 26–31, https://doi.org/10.1016/j.scriptamat.2020.10.003.
[38] A. Walnsch, M.J. Kriegel, P.D.B. Fischer, S. Neumann, D. Rafaja, A. Leineweber, Nanoscale twinning and superstructures of martensite in the Fe–Mn–Al–Ni system, Materialia 16 (2021) 101062, https://doi.org/10.1016/j.mtla.2021.101062.